Hydrogenated Graphene as a Homoepitaxial Tunnel Barrier for Spin and Charge Transport in Graphene

Adam L. Friedman,[*,†] Olaf M. J. van 't Erve,[†] Jeremy T. Robinson,[‡] Keith E. Whitener, Jr.,[§] and Berend T. Jonker[†]

[†]Materials Science and Technology Division, [‡]Electronics Science and Technology Division, and [§]Chemistry Division, Naval Research Laboratory, Washington, D.C. 20375, United States

ABSTRACT

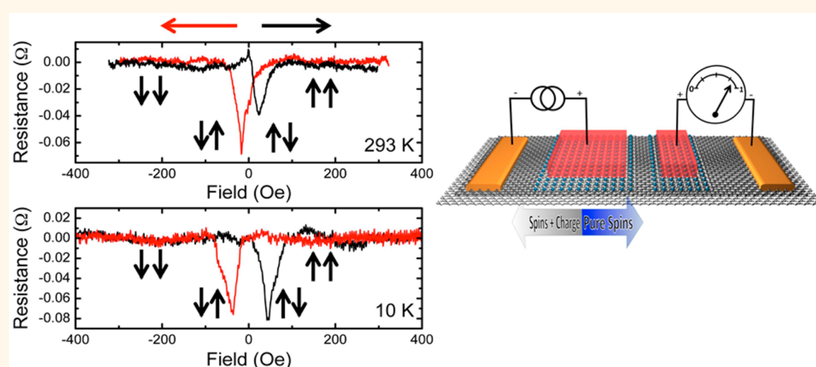

We demonstrate that hydrogenated graphene performs as a homoepitaxial tunnel barrier on a graphene charge/spin channel. We examine the tunneling behavior through measuring the *IV* curves and zero bias resistance. We also fabricate hydrogenated graphene/graphene nonlocal spin valves and measure the spin lifetimes using the Hanle effect, with spintronic nonlocal spin valve operation demonstrated up to room temperature. We show that while hydrogenated graphene indeed allows for spin transport in graphene and has many advantages over oxide tunnel barriers, it does not perform as well as similar fluorinated graphene/graphene devices, possibly due to the presence of magnetic moments in the hydrogenated graphene that act as spin scatterers.

KEYWORDS: graphene · hydrogenated graphene · electronic transport · spin transport · tunnel barrier

In spite of nearly a decade of research on spin transport in graphene,[1,2] there has been little improvement in important metrics such as the spin lifetime and spin diffusion length,[3,4] and reported values remain far below those predicted by theory based on graphene's low atomic number and spin–orbit coupling.[5] Understanding the extrinsic limiting factors and achieving the theoretically predicted values of these metrics is key for enabling the type of advanced, low-power, high-performance spintronic devices envisioned beyond Moore's law.[6,7]

Several sources of scattering give rise to the lower spin lifetimes experimentally observed in graphene: scattering caused by charges in the substrate,[8] scattering caused by grain boundaries, defects, and impurities in the graphene or at the contacts,[4,9] and scattering introduced by the tunnel barrier. Limits in performance due to substrate scattering are now appreciated, and solutions are being developed. For example, recent research shows that high-*k* dielectrics and monolayer BN can provide the best substrates for graphene,[10] considerably reducing the parasitic effects of phonon scattering and scattering by trapped charge in the substrate. Scattering caused by defects and impurities is also being addressed. Defect-free graphene films are now grown with millimeter size grains,[11] and methods such as deep-UV lithography and dry and *in situ* processing are reducing or eliminating processing-related contamination issues.[12,13]

* Address correspondence to adam.friedman@nrl.navy.mil.

Received for review May 8, 2015 and accepted June 5, 2015.

Published online June 05, 2015
10.1021/acsnano.5b02795

This article not subject to U.S. Copyright. Published 2015 by the American Chemical Society

Finally, scattering caused by tunnel barriers, which are essential for solving the conductivity mismatch problem for electrical spin injection from a ferromagnetic metal[14] into a semiconductor, is a topic that is just now attracting attention. Uniform, pinhole-/defect-free tunnel barriers on graphene are not easily attained with the conventional methods that use oxides.

Recent studies using pinhole-free, high-resistance tunnel barriers (*e.g.*, monolayer BN[15] and amorphous carbon[16]) that minimally affect the graphene surface showed enhanced metrics for spin transport in graphene over previous work using conventional oxide tunnel barriers.[17,18] Graphene itself exhibits many of the characteristics expected from a perfect tunnel barrier, including discrete monolayer thickness, imperviousness to interdiffusion, high uniformity, and high out-of-plane resistance, offering a new paradigm for tunnel barriers in magnetic tunnel junctions and spin injection into silicon.[19,20] Moreover, in a graphene bilayer, by electrically decoupling the top layer from the bottom using chemical functionalization,[21] a fluorographene/graphene homoepitaxial tunnel barrier structure showed the highest spin polarization achieved in graphene.[22] Such functionalized homoepitaxial structures provide an elegant approach for realization of graphene-based spintronic devices, although spin-dependent operation was not achieved at room temperature, and fluorinated graphene has reduced stability compared to conventional dielectric materials.

Hydrogenation of graphene offers an alternative method to achieve a homoepitaxial tunnel barrier on graphene. In contrast with fluorination[23] and plasma treatments,[24] the Birch reduction hydrogenation process we employ provides a rapid, gentler, and more stable functionalization with much higher hydrogen coverage.[25] Recent experimental[26] and theoretical[27] studies show that hydrogenated graphene could be magnetic, which could be used to control spin relaxation in the graphene.[9,28,29]

Here we show that hydrogenated graphene serves as an effective spin tunnel barrier for graphene up to room temperature. Beginning with a multilayer stack of graphene, we hydrogenate the top layers to create a tunnel barrier and demonstrate electrical spin injection, transport, precessional dephasing, and detection in the lower graphene channel layers using the four-terminal nonlocal spin valve (NLSV) geometry. We extract spin lifetimes from the Hanle effect measurements and polarization efficiencies from the NLSV measurements and compare these results to those found for fluorographene/graphene homoepitaxial devices.

RESULTS AND DISCUSSION

Graphene is grown by chemical vapor deposition (CVD) on Cu foils (see Methods section). Using conventional wet chemical transfer techniques,[21] four single-layer graphene films are successively transferred onto a SiO_2/Si substrate. Four-terminal nonlocal spin valve structures are fabricated using deep-UV lithography with PMMA resist and acetone rinses. Mesas are defined by etching in O_2 plasma. Ti/Au reference contacts are applied by lift-off using electron beam deposition. The edges of the graphene are encapsulated by a sputtered Si_3N_4 layer before hydrogenation *via* the Birch reduction process to reduce intercalation and functionalization of the bottom graphene layer(s). Figure 1a shows an optical image of a completed device, and Figure 1b shows a cartoon schematic of a completed device in an NLSV measurement configuration, used later in the study.

Figure 1c shows Raman spectra of an as-fabricated four-layer graphene structure with the characteristic D (1350 cm^{-1}), G ($\sim$1600 cm^{-1}), and 2D ($\sim$2700 cm^{-1}) peaks. The D peak intensity, which is associated with defects,[30] is minimal in as-fabricated structures and indicates that high-quality graphene multilayer devices can be realized even after several sequential transfers. The crystalline orientation between each graphene layer, or twist angle (θ), determines the relative degree of electronic coupling between layers. When clean interfaces are present in stacked graphene films, electronic coupling can be measured *via* Raman spectroscopy, where the G and 2D peak intensities vary by known quantities with twist angle.[21] The black curve in the spectrum in Figure 1c highlights a "large" twist angle ($\theta > 16°$) domain, which was taken from spot 1 of the accompanying Raman micrograph, where the color code corresponds to the integrated G peak intensity. The red curve in the spectrum, taken from spot 2, highlights a resonant twist angle, caused by electronic coupling between the graphene layers. After hydrogenation by the Birch reduction process (see Methods), we see the emergence of the D peak and the base of the G peak broadens (Figure 1d), indicating that hydrogen functionalization has occurred. On the basis of the continued presence of a sharp G and 2D peak after hydrogenation, we interpret the resulting spectra as a linear combination of hydrogenated graphene layers and pristine bottom graphene layers. In addition, the corresponding integrated G peak intensity micrograph shows an accompanying change in interlayer electronic interaction caused by the hydrogenation. We still observe electronic coupling, demonstrated by the resonant twist angle spectrum (Figure 1d, red curve, spot 2), proving that hydrogenation has occurred only in the top graphene layers, leaving the bottom two layers mostly unfunctionalized.

After the four-layer channel is converted to top hydrogenated and bottom pristine graphene layers, two $Ni_{80}Fe_{20}$ (Py) contacts (1 and 3 μm wide, separated by 1 μm) for spin injection/detection are deposited by electron beam evaporation. These contacts (or "pins")

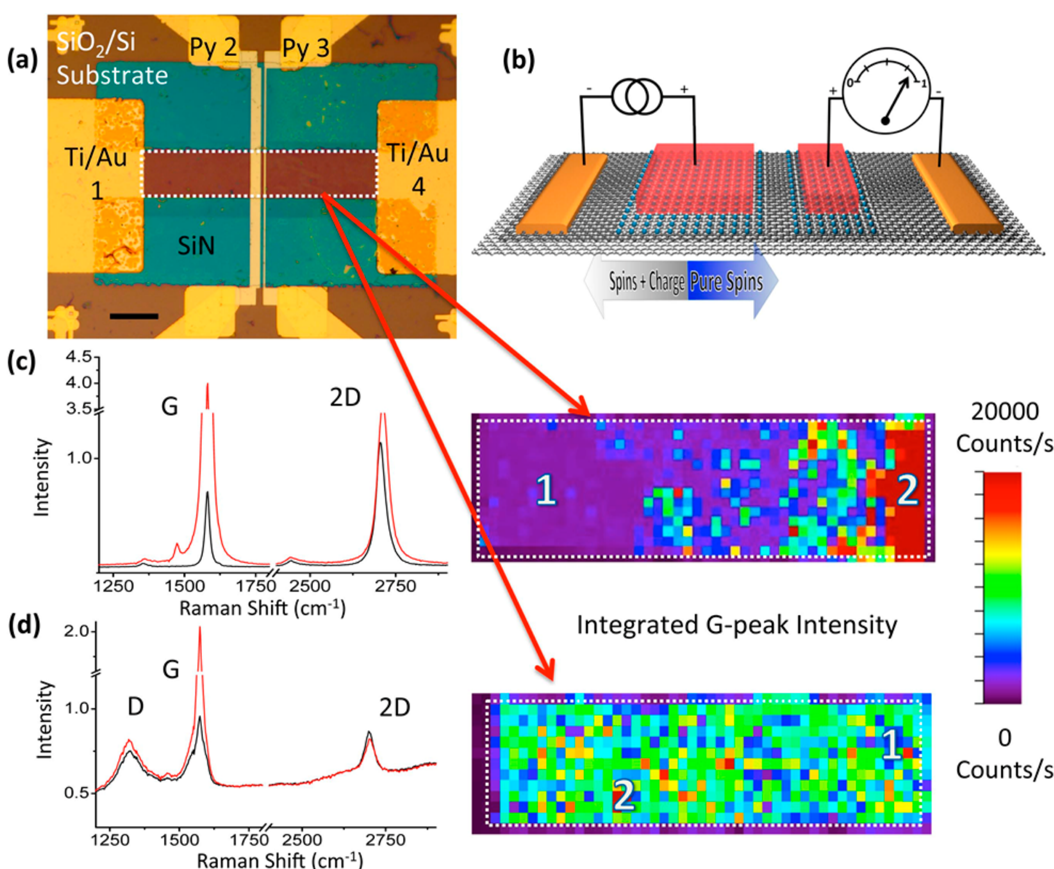

Figure 1. (a) Optical microscope image of a four-terminal graphene device. The white dotted line outlines the four-layer graphene channel (scale bar = 15 μm). (b) Cartoon schematic of a device configured in a nonlocal spin valve geometry. (c) Raman spectra and integrated G peak intensity map of a four-layer graphene device channel as shown in (a). The black and red spectra are taken from points 1 and 2, respectively, from the Raman map and identify a "large" and "resonant" twist angle (λ = 488 nm). (d) Raman spectra and integrated G peak intensity map of a different four-layer graphene device after hydrogenation. The black and red spectra are taken from points 1 and 2, respectively, from the Raman map and also identify a "large" and "resonant" twist angle domain. The appearance of a D defect peak and continued observation of resonance indicate that the top graphene layers have been hydrogenated and that the lower graphene layer has not been hydrogenated.

are written using an electron beam lithography defined PMMA mask to form the NLSV structure illustrated in Figure 1b. The pins are numbered in Figure 1a for later reference. Most electrical measurements are performed in a variable-temperature, cryogen-free cryostat/electromagnet system. Further device preparation procedures can be found in the Methods section.

To test for tunneling behavior in the device, we perform charge transport measurements. The red curve in Figure 2 shows the resistance measured between the Ti/Au contacts (1 and 4 in Figure 1a) *vs* back gate voltage and a Dirac point at ~90 V before hydrogenation, indicating a very conductive structure with strong p-type doping. This doping is most likely due to impurities adsorbed on the graphene surface. After hydrogenation of the top layers, the same measurement (Figure 2, black curve) shows a Dirac point at ~10 V, which we attribute to conduction in the bottom graphene layers. In contrast with fluorination, which creates very strongly p-type graphene devices when

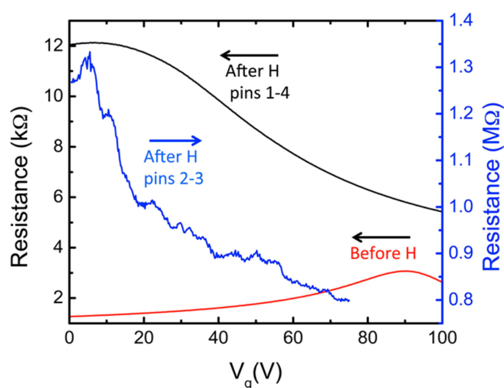

Figure 2. Resistance *vs* gate voltage for the device before hydrogenation (red), after hydrogenation for contacts 1 and 4, nominally only on the conductive channel (black), and after hydrogenation for contacts 2 and 3, nominally only on the resistive tunnel barrier portion of the device. The Dirac point shifts from ~90 V before hydrogenation to ~10 V after hydrogenation, expected due to n-doping by hydrogen. The differences in resistance between the curves taken between contacts 1–4 and 2–3 indicate electrical separation of the graphene layers necessary for tunneling.

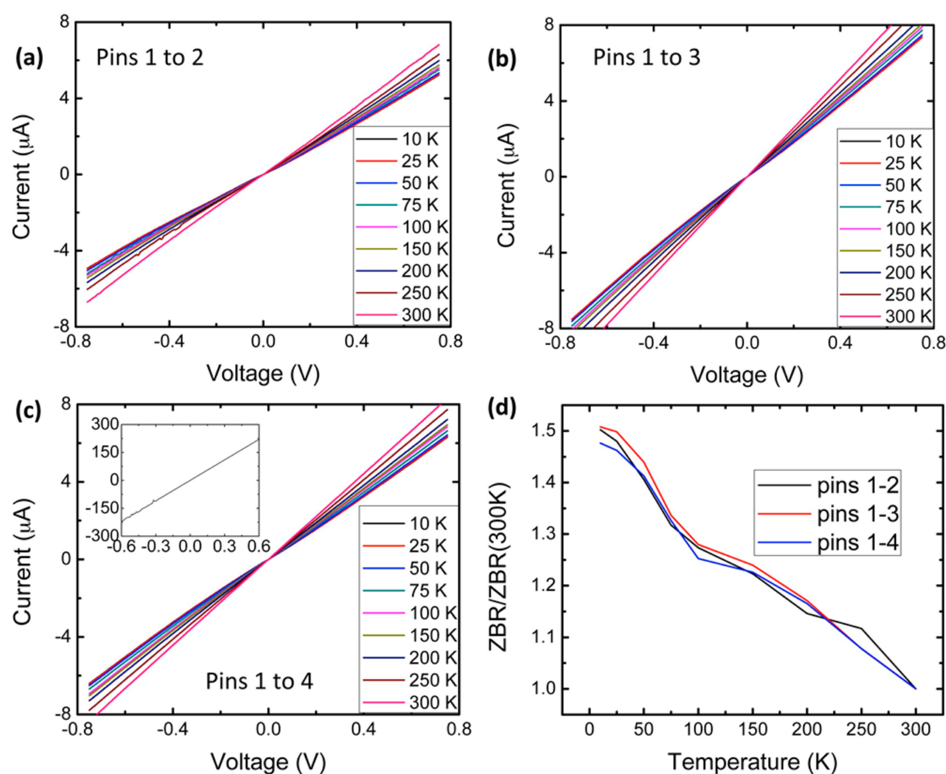

Figure 3. ***IV*** **curves displaying non-ohmic behavior for increasing temperature for (a) pins 1 to 2, (b) pins 1 to 3, and (c) pins 1 to 4. Inset shows that the** ***IV*** **curve before hydrogenation is ohmic. The resistance again increases after hydrogenation, indicating that the hydrogen diffuses under the contact, making all contacts tunneling. (d) The zero-bias resistance as a function of temperature for all contacts. Weak temperature dependence indicates tunneling transport.**

combined in a fluorographene/graphene stack,[22] hydrogenation is known to create n-type devices.[31] Such n-type doping would be expected to shift the Dirac point to lower values.

The resistance of the channel between the Ti/Au contacts increases after hydrogenation (~3.5 kΩ to ~12 kΩ at the Dirac point for this device), which is to be expected, as the top graphene layers are turned insulating from hydrogenation. A concurrently hydrogenated single layer of graphene has a resistance of ~45 GΩ, indicating that the hydrogenation creates an insulator in the top layers of our device and conduction occurs in the lower unhydrogenated layer(s) by first tunneling through the hydrogenated graphene.

The transistor characteristics measured between the two Py contacts (pins 2 and 3 in Figure 1a), *i.e.* only contacting the top hydrogenated graphene film (Figure 2, blue curve), show 2 orders-of-magnitude higher resistance than the measurements between the Ti/Au contacts. This increased resistance, together with the fact that single graphene layer treated at the same time has greater than gigaohm resistance, supports electrical transport between the Py contacts points to tunneling. However, it does not indicate the complete electrical separation of the layers observed in fluorographene/graphene homostructures.[21,22] All devices measured displayed similar resistance *vs* back gate voltage characteristics.

Figure 3a and b show *IV* curves taken between the Py (pins 2 and 3) and a reference Ti/Au contact (pin 1). These curves exhibit markedly non-ohmic behavior, which provides support that the hydrogenated graphene is acting as a tunnel barrier. For *IV* curves taken between the two Ti/Au reference contacts (pins 1 to 4, Figure 3c), we unexpectedly see non-ohmic behavior and high resistance. This, plus our observation of a varying amount of resistance increase between the Ti/Au from device to device, strongly suggests that some hydrogenation occurred under the Ti/Au contacts, most likely through intercalation. Of all devices tested, most showed this behavior, with the reference contacts increasing in resistance by at least an order-of-magnitude and losing their ohmic *IV* behavior after hydrogenation. The inset of Figure 3c shows an *IV* curve taken between these pins before hydrogenation, which shows the expected ohmic behavior. The temperature dependence of the zero bias resistance for both Py and Ti/Au contacts (Figure 3d) is weak and insulator-like in character, changing by a factor ~1.5 between 5 and 300 K for all contacts in the device. Non-ohmic *IV* curves and a weakly temperature-dependent zero-bias resistance is a firm confirmation of a pinhole-free tunnel barrier.[32]

The four-terminal (4T) NLSV geometry was used to generate pure spin currents. In NLSV measurements, a bias current is applied between one of the ferromagnetic

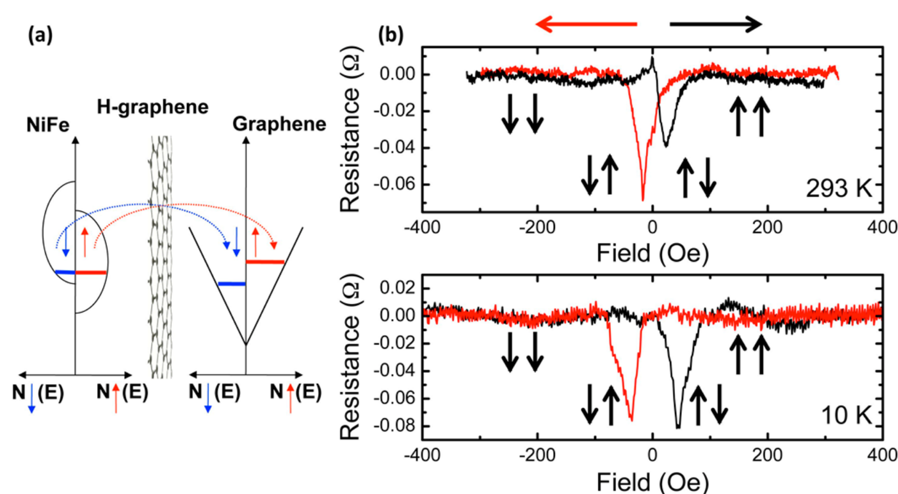

Figure 4. (a) Energy diagrams for polarized spin tunneling. Spins from the Py tunnel across the hydrogenated graphene and into available states in the graphene. (b) NLSV at 10 K (lower graph) and 293 K (upper graph) and a −10 μA bias current. The red curve is for sweeping the field from negative to positive, and the black curve is for sweeping the field from positive to negative, as indicated by the directions of the colored arrows above the plot. The black arrows inside the plots indicate the relative magnetic orientations of the contacts. A ∼150 Ω background signal has been subtracted from the data.

(FM, here Py) contacts and the nearest reference contact, and a spin-polarized charge current is injected from the FM across the hydrogenated graphene tunnel barrier and into the graphene transport channel. Figure 4a depicts this in an energy diagram. This spin-charge current follows the electric field and flows as shown in Figure 1b. Spin simultaneously diffuses in all directions, creating a pure spin current, and the corresponding spin accumulation results in a spin-splitting of the chemical potential. This is manifested as a voltage on the second FM contact, which is outside of the charge current path and referred to as the nonlocal detector. An in-plane magnetic field is used to control the relative orientation of the magnetizations of the FM injector and detector contacts. When the magnetizations are parallel, the voltage measured will be smaller than when they are antiparallel. Sweeping the magnetic field causes the contact magnetizations to reverse in plane at their respective coercive fields and produce a measurable voltage peak. In order to observe this effect, we fabricate the FM contacts with two different widths (1 and 3 μm) to exploit magnetic shape anisotropy so that the coercivities of the ferromagnetic contacts are different.

This NLSV behavior is clearly observed in Figure 4b at 10 K, where distinct steps in the nonlocal resistance (the measured detector voltage divided by the bias current) appear at the coercive fields of the wide and narrow FM contacts, producing plateaus of higher resistance when the FM contact magnetizations are antiparallel. This behavior persists to room temperature, with only a 50% decrease in magnitude observed from 10 to 293 K, as shown in Figure 4b. The coercive fields decrease slightly with increasing temperature, so that the two individual peaks are not as well separated for our choice of contact geometric parameters. These data demonstrate successful spin injection and detection at the FM/hydrogenated graphene tunnel contacts and lateral spin transport in the graphene channel.

The spin lifetime corresponding to this pure spin current is quantitatively determined using the Hanle effect,[33] in which a magnetic field B_z applied along the surface normal causes the spins in the graphene transport channel to precess at the Larmor frequency, $\omega_L = g\mu_B B_z/\hbar$, and dephase. Here g is the Lande g-factor ($g \approx 2$ for graphene), μ_B is the Bohr magneton, and $\hbar$ is Planck's constant. As the magnetic field increases, the net spin polarization and corresponding spin voltage decrease to zero with a characteristic pseudo-Lorentzian line shape. Figure 5a shows a Hanle spin precession curve for the four-terminal nonlocal contact geometry. The blue line in Figure 5a shows a scan taken from a concurrently fabricated witness device in which the graphene was not hydrogenated. We note that no NLSV signal or Hanle effect is apparent in such witness samples, demonstrating that the hydrogenated graphene tunnel barrier is necessary to achieve spin injection.

The measured Hanle signal is directly proportional to the steady-state spin polarization at the detector, given by[34]

$$S(x_1, x_2, B_z) = S_0 \int_0^\infty \frac{1}{\sqrt{4\pi Dt}} e^{-(x_2 - x_1 - v_d t)^2/4Dt} \cos(\omega_L t) e^{-t/t_s}\, dt \quad (1)$$

where spin is injected into the graphene at x_1 and $t = 0$ and detected at x_2. S_0 is the spin injection rate, D is the electron diffusion constant, v_d is the electron drift velocity (=0 for diffusive transport), and t_s is the spin lifetime. Fits to the data (Figure 5a, shown in red) provide a measure of the spin lifetime. For the device

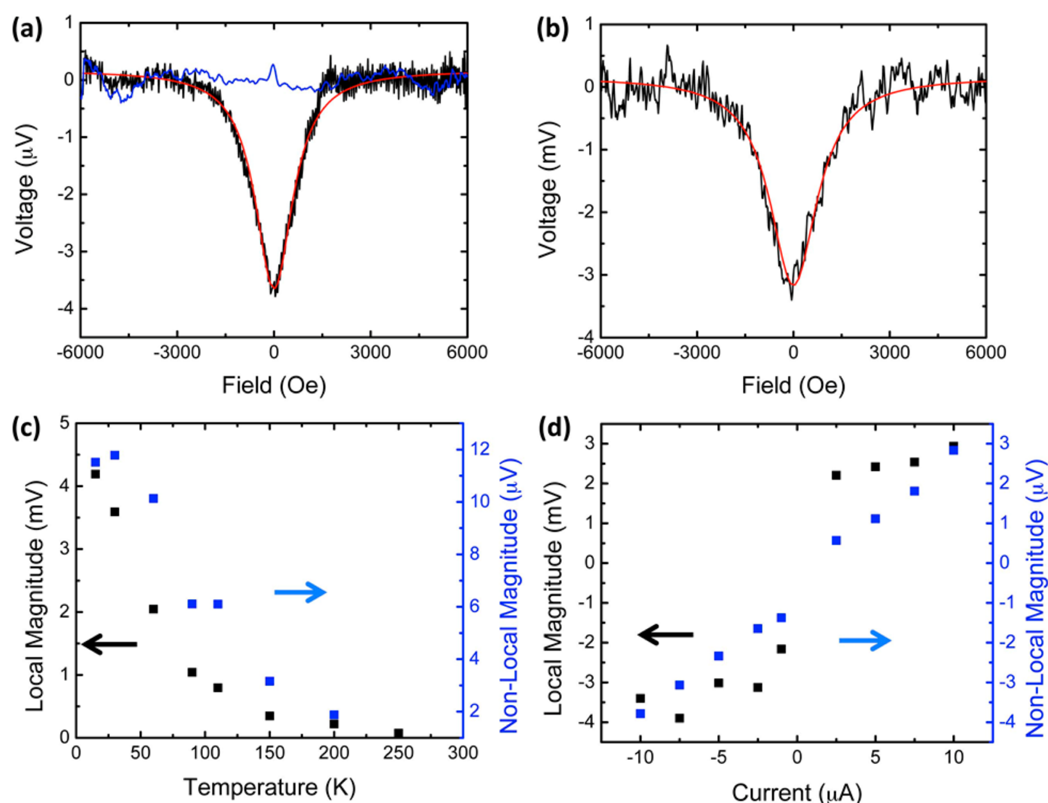

Figure 5. (a) 4T nonlocal Hanle effect taken at 10 K and with a −10 μA bias. The black line shows the data. The red line is the theoretical fit, from which a spin lifetime of ∼70 ps and spin diffusion length of ∼2 μm are extracted. The blue line is a witness sample showing no Hanle signal, indicating that the hydrogenated graphene is necessary to achieve spin transport. (b) Two-terminal Hanle effect taken at 10 K and with a −10 μA bias. The red line is the theoretical fit to a pseudo-Lorentzian line shape from which a spin lifetime of ∼65 ps is extracted. (c) Temperature dependence of the magnitude of the local and nonlocal Hanle effects. Hanle signal persists to ∼250 K. (d) Bias dependence of the local and nonlocal Hanle effects, showing the expected near-linear (2T) and linear (4T) relationship and sign reversal.

pictured here, at a bias current of −10 μA and temperature of 10 K, 4T spin lifetimes were ∼70 ps. The spin diffusion length is given by $L_{SD} = (Dt_s)^{1/2}$, where D is the diffusion constant.[35] We find an average $L_{SD} \approx$ 2 μm, based on $t_s \approx$ 70 ps and $D \approx 0.069\ m^2/s$ at 10 K, consistent with other studies of CVD-grown graphene films.[36] The spin lifetime and spin diffusion length shows no dependence on the gate voltage. This is contrary to the expected spin lifetime increase with increased carrier doping[37,38] and to what is observed in fluorographene tunnel barrier devices.[22] However, this behavior is similar to what is observed in oxide tunnel barrier/graphene heterostructures.[3] It is most likely due to the low resistance of the tunnel barrier.[1,3] Additionally, according to theory, the magnitude of the Hanle signal should be approximately half that of the NLSV signal. At this time we do not understand the discrepancy; however, it could be caused by non-saturating magnetic moments in the contacts.

Additionally, the spin current can be injected and the spin voltage detected with the same Py contact in a local, two-terminal (2T) configuration, shown in Figure 5b. Here, we measure the spin accumulation and lifetime directly under the Py contact (locally). The voltage $\Delta V_{2T}(B_z)$ decreases with B_z with a pseudo-Lorentzian line shape given by $\Delta V_{2T}(B_z) = \Delta V_{2T}(0)/[1 + (\omega_L t_s)^2]$.[39] In this way, fits to the Hanle curves, shown in Figure 5b in red, allow us to extract the 2T spin lifetime, found to be ∼65 ps, which is consistent with the nonlocal data.

Figure 5c shows the temperature dependence of the Hanle effect with the blue squares representing the 4T nonlocal Hanle effect data (right axis, as indicated by the blue arrow) and the black squares representing the 2T Hanle effect data (using the left axis, as indicated by the black arrow). The Hanle signal persists up to ∼250 K, higher than for fluorographene tunnel barriers (∼200 K).[22] We found that the spin lifetime remains mostly unchanged as a function of temperature.

Figure 5d shows the bias dependence of the magnitude of the 4T nonlocal (blue squares, right axis) and 2T local (black squares, left axis) Hanle voltage taken at $B = 0$. The 2T data are slightly nonlinear, and the 4T are approximately linear with bias current, as expected and consistent with other studies.[20,22] We also observe that the sign of the Hanle signal inverts as the sign of the bias current changes, a firm confirmation that our observed signal is due to Hanle spin precession. The observation of both the nonlocal Hanle effect and the NLSV provides strong evidence that the hydrogenated

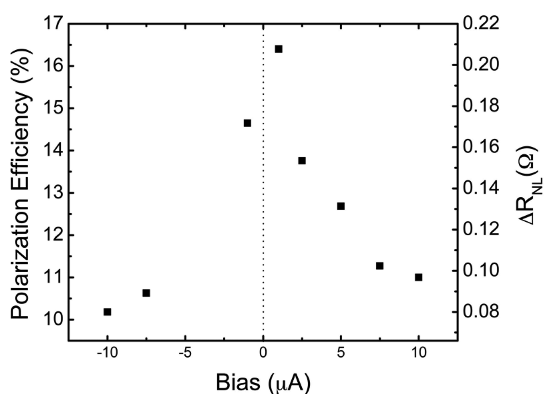

Figure 6. Measured magnitude of the NLSV peak and calculated polarization efficiency as a function of sample bias taken at 10 K.

graphene tunnel barrier indeed enables efficient spin injection, transport, and detection in the graphene channel.

Overall, the spin lifetime values measured for both the 4T and 2T cases are in the lower range of other graphene spin studies and significantly less than what was measured for fluorinated graphene tunnel barriers. Recent work has suggested that magnetic impurities, which we expect for hydrogenated graphene, can be the primary source of spin relaxation[9] and could be causing the shorter than expected spin lifetimes. There is ample evidence to support that both fluorinated graphene[40] and hydrogenated graphene can be magnetic[41] and that this magnetism could affect the spin transport.[42] For fluorinated graphene, expected paramagnetic moments that could contribute to spin scattering are at a minimum for negative doping away from the Dirac point,[38] as is the case in ref 22. For the hydrogenated graphene used as a tunnel barrier here, the type of magnetism is strongly dependent on substrate-hydrogenated graphene interactions and the degree of functionalization.[41] The cause and type of magnetism are still a matter of debate, even though most agree it persists to at least room temperature.[27,43] Moreover, for hydrogenated graphene, spin scattering is enhanced by the persistence of the magnetic moments for carrier doping away from the Dirac point.[38] The hydrogenated graphene has its moment oriented out-of-plane and could be either paramagnetic or ferromagnetic. In the case of paramagnetic moments, for a Hanle measurement with an applied field out-of-plane, the moments would scatter the spins in the channel, decreasing the spin lifetime and observed signal magnitude. As the temperature is increased, this effect would get worse. For an NLSV, with the external field applied in-plane, the moments would align in-plane with the applied field, again causing scattering and lowering the spin lifetime. In the case of ferromagnetic moments oriented out-of-plane, the spins in the channel and the out-of-plane spins from the graphene will start to align due to spin-torque transfer, resulting in more scattering of the spin current. Therefore, in either case, magnetism in the hydrogenated graphene tunnel barrier could be the cause of the lower spin lifetimes and the lack of Hanle signal at room temperature.

Based on the magnitude of the NLSV signal and the calculated spin diffusion length from the Hanle measurements, we can determine the spin polarization efficiency, P, using the formula[44]

$$R_{\mathrm{nonlocal}} = \frac{P^2 L_{\mathrm{SD}}}{W\sigma} \exp(-L/L_{\mathrm{SD}}) \qquad (2)$$

where the σ is the measured conductivity of $2.83 \times 10^{-3}\ \Omega^{-1}$ for the device shown in Figure 4, L is the center-to-center contact spacing of 3 μm, L_{SD} is the spin diffusion length of 2 μm, W is the width of the graphene channel of 15 μm, and R_{nonlocal} is the magnitude of the NLSV plateau of $\sim$0.08 Ω. From this, we find $P \approx 10\%$. Figure 6 summarizes the magnitude of the NLSV peak and the calculated polarization efficiency as a function of bias. The nonlinear increase of the polarization efficiency and the NLSV resistance with a decrease in bias are typical of NLSV devices.[45,22] The maximum low-bias spin polarization measured here of $\sim$16.5% is significantly lower than the 45% measured in fluorographene tunnel barriers,[22] although still high for graphene devices.[1,17] A possible reason for the lower spin polarization could be scattering by persistent magnetic moments in the tunnel barrier.

CONCLUSION

In conclusion, we have demonstrated that the hydrogenated graphene serves as a tunnel barrier enabling tunneling transport and spin injection/detection in a graphene channel. On the basis of polarization efficiency values, low spin lifetime, and the absence of strong gate-modulated spin transport, we can conclude that the hydrogenated graphene tunnel barriers do not perform as well as similar fluorinated graphene tunnel barriers. However, because the hydrogenation process results in a more stable functionalized graphene sheet and displays spin signal even up to room temperature, it is nonetheless still a reasonable candidate for future graphene spintronic devices.

METHODS

Graphene was grown by chemical vapor deposition *via* decomposition of methane in small Cu foil enclosures following methods available in the literature.[11] This method produces monolayer graphene films with grain sizes on the order of hundreds of micrometers containing minimal defects. After growth, the Cu foil is removed by etching and four graphene

layers are transferred and stacked using previously reported techniques known to produce high-quality, clean multilayer stacks.[21] We found that four stacked layers are the minimum required to ensure that after hydrogenation there is still a conductive channel in the stack. Deep-UV lithography is used with PMMA followed by oxygen plasma to define square graphene mesas. PMMA was found to leave less residual dirt on the surface of the films than standard photolithography resists. The sample is rinsed in acetone and isopropyl alcohol to remove the etch mask. Reference contacts and bond pads are then defined using an MMA/PMMA mask with features defined using deep-UV lithography. Ti/Au is deposited using electron beam deposition and lift-off in acetone. One more MMA/PMMA mask with deep-UV lithography, followed by sputter deposition of 10 nm of Si_3N_4, is used to encapsulate the edges of the four-layer graphene, attempting to prevent hydrogen from getting underneath the graphene.

The sample is then hydrogenated using the Birch reduction process, described in detail elsewhere.[25] Briefly, graphene samples were added to 10 mL of liquid ammonia at −78 °C. Lithium wire (50 mg) was added in small pieces to the reaction, and the vessel was swirled to homogenize the resultant blue color. After 2 min, the reaction was quenched by adding an excess of ethanol slowly while continuously swirling to prevent the reaction from bubbling over. The wafer was removed from the vessel, rinsed with more ethanol, and dried under N_2. We attempted to perform this hydrogenation with two- and three-layer stacks. A bilayer of graphene is completely hydrogenated, thus electrically insulating and unusable for this experiment. A trilayer of graphene has the first two layers completely hydrogenated and the third layer mostly hydrogenated, again yielding an insulating channel, unusable for this experiment. Four layers is the thinnest stack that still presents a complete conducting path of unhydrogenated graphene underneath the upper hydrogenated layers. We suspect that hydrogen intercalates between layers through edges, defects, and grain boundaries in the graphene. Concurrently hydrogenated single layer and bilayer devices show a resistance of ∼45 GΩ after hydrogenation, indicating that at least the top two layers of graphene are completely insulating after hydrogenation.

A final mask of PMMA is spun on the sample, and electron beam lithography is used to define trenches for electron beam deposition and lift off of 25 nm $Ni_{80}Fe_{20}$/5 nm Au contacts that act as spin-polarized injectors/detectors.

Conflict of Interest: The authors declare no competing financial interest.

Acknowledgment. The authors thank David Zapotok and Dean St. Amand of the NRL Nanoscience Institute for technical assistance. The authors gratefully acknowledge support from the NRL 6.1 core science program, the NRL Nanoscience Institute basic research program, and the Air Force Office of Scientific Research under contract number F4GGA24233G001.

REFERENCES AND NOTES

1. Tombros, N.; Jozsa, C.; Popinciuc, M.; Jonkman, H. T.; van Wees, B. J. Electronic Spin Transport and Spin Precession in Single Graphene Layers at Room Temperature. *Nature* **2007**, *448*, 571–574.
2. Han, W.; Kawakami, R. K.; Gmitra, M.; Fabian, J. Graphene Spintronics. *Nat. Nanotechnol.* **2014**, *9*, 794–807.
3. Volmer, F.; Drogeler, M.; Maynicke, E.; von den Driesch, N.; Boschen, M. L.; Guntherodt, G.; Beschoten, B. Role of MgO Barriers for Spin and Charge Transport in Co/MgO/Graphene Nonlocal Spin-Valve Devices. *Phys. Rev. B* **2013**, *88*, 161405(R).
4. Sosenko, E.; Wei, H.; Aji, V. Effect of Contacts on Spin Lifetime Measurements in Graphene. *Phys. Rev. B* **2014**, *89*, 245436.
5. Pesin, D.; MacDonald, A. H.; Spintronics and Pseudospintronics in Graphene and Topological Insulators. *Nat. Mater.* **2012**, *11*, 409–416.
6. International Technology Roadmap for Semiconductors, "Emerging Materials", **2013**, www.itrs.net.
7. Dery, H.; Wu, H.; Ciftcioglu, B.; Huang, M.; Song, Y.; Kawakami, R.; Shi, J.; Krivorotov, I.; Zutic, I.; Sham, L. J. Nanospintronics Based on Magnetological Gates. *IEEE Trans. Electron Devices* **2011**, *59*, 259–262.
8. Cress, C. D.; Champlain, J. G.; Esqueda, I. S.; Robinson, J. T.; Friedman, A. L.; McMorrow, J. J. Total Ionizing Dose Induced Charge Carrier Scattering in Graphene Devices. *IEEE Trans. Nucl. Sci.* **2012**, *59*, 3045–3053.
9. Kochan, D.; Gmitra, M.; Fabian, J. Spin Relaxation Mechanism in Graphene: Resonant Scattering by Magnetic Impurities. *Phys. Rev. Lett.* **2014**, *112*, 116602.
10. Kretinin, A. V.; Cao, Y.; Tu, J. S.; Yu, G. L.; Jalil, R.; Novoselov, K. S.; Haigh, S. J.; Gholinia, A.; Mishchenko, A.; Lozada, M.; *et al*. Electronic Properties of Graphene Encapsulated with Different Two-Dimensional Atomic Crystals. *Nano Lett.* **2014**, *14*, 3279–3276.
11. Li, X.; Magnuson, C. W.; Venugopal, A.; Tromp, R. M.; Hannon, J. B.; Vogel, E. M.; Colombo, L.; Ruoff, R. S. Large-Area Graphene Single Crystals Grown by Low-Pressure Chemical Vapor Deposition of Methane on Copper. *J. Am. Chem. Soc.* **2011**, *133*, 2816–2819.
12. Drogeler, M.; Volmer, F.; Wolter, M.; Terres, B.; Watanabe, K.; Taniguchi, T.; Guntherodt, G.; Stamfer, C.; Beschoten, B. Nanosecond Spin Lifetimes in Single- and Few-Layer Graphene-hBN Heterostructures at Room Temperature. *Nano Lett.* **2014**, *14*, 6050–6055.
13. Castellanos-Gomez, A.; Buscema, M.; Molenaar, R.; Singh, V.; Janssen, L.; van der Zant, H. S. J.; Steele, G. A. Deterministic Transfer of Two-Dimensional Materials by All-Dry Viscoelastic Stamping. *2D Mater.* **2014**, *1*, 011002.
14. Fert, A.; Jaffres, H. Conditions for Efficient Spin Injection from a Ferromagnetic Metal into a Semiconductor. *Phys. Rev. B* **2001**, *64*, 184420.
15. Yamaguchi, T.; Inoue, Y.; Masubuchi, S.; Morikawa, S.; Onuki, M.; Watanabe, K.; Taniguchi, T.; Moriya, R.; Machida, T. Electrical Spin Injection into Graphene through Monolayer Hexagonal Boron Nitride. *Appl. Phys. Express* **2013**, *6*, 073001.
16. Neumann, I.; Costach, M. V.; Bridoux, G.; Sierra, J. F.; Valenzuela, S. O. Enhanced Spin Accumulation at Room Temperature in Graphene Spin Valves with Amorphous Carbon Interfacial Layers. *Appl. Phys. Lett.* **2013**, *103*, 112401.
17. Han, W.; Pi, K.; McCreary, K. M.; Li, Y.; Wong, J. J. I.; Swartz, A. G.; Kawakami, R. K. Tunneling Spin Injection into Single Layer Graphene. *Phys. Rev. Lett.* **2010**, *105*, 167202.
18. Dlubak, B.; Seneor, P.; Anane, A.; Barraud, C.; Deranlot, C.; Deneuve, D.; Servet, B.; Mattana, R.; Petroff, F.; Fert, A. Are Al_2O_3 and MgO Tunnel Barriers Suitable for Spin Injection in Graphene? *Appl. Phys. Lett.* **2010**, *97*, 092502.
19. Cobas, E.; Friedman, A. L.; van 't Erve, O. M. J.; Robinson, J. T.; Jonker, B. T. Graphene-Based Magnetic Tunnel Junctions. *Nano Lett.* **2012**, *12*, 3000–3004.
20. van 't Erve, O. M. J.; Friedman, A. L.; Cobas, E.; Li, C. H.; Robinson, J. T.; Jonker, B. T. Low-Resistance Spin Injection into Silicon Using Graphene Tunnel Barriers. *Nat. Nanotechnol.* **2012**, *7*, 737–742.
21. Robinson, J. T.; Schmucker, S. W.; Biaconescu, C. B.; Long, J. P.; Culbertson, J. C.; Ohta, T.; Friedman, A. L.; Beechem, T. E. Electronic Hybridization of Large-Area Stacked Graphene Films. *ACS Nano* **2013**, *7*, 637–644.
22. Friedman, A. L.; van 't Erve, O. M. J.; Li, C. H.; Robinson, J. T.; Jonker, B. T. Homoepitaxial Tunnel Barriers with Functionalized Graphene-on-Graphene for Charge and Spin Transport. *Nat. Commun.* **2014**, *5*, 4161. In this reference, the calculated low-bias polarization efficiency is ∼45% using the formula found in ref 44 (eq 2).
23. Stine, R.; Lee, W. K.; Whitener, K. E., Jr.; Robinson, J. T.; Sheehan, P. E. Chemical Stability of Graphene Fluoride Produced by Exposure to XeF_2. *Nano Lett.* **2013**, *13*, 4311–4316.
24. Matis, B. R.; Burgess, J. S.; Bulat, F. A.; Friedman, A. L.; Houston, B. H.; Baldwin, J. W. Surface Doping and Band Gap Tunability in Hydrogenated Graphene. *ACS Nano* **2012**, *6*, 17–22.

25. Whitener, K. E., Jr.; Lee, W. K.; Campbell, P. M.; Robinson, J. T.; Sheehan, P. E. Chemical Hydrogenation of Single-Layer Graphene Enables Completely Reversible Removal of Electrical Conductivity. *Carbon* **2014**, *72*, 348–353.
26. Giesbers, A. J. M.; Uhlirova, K.; Konecny, M.; Peters, E. C.; Burghard, M.; Aarts, J.; Flips, C. F. J. Interface-Induced Room Temperature Ferromagnetism in Hydrogenated Epitaxial Graphene. *Phys. Rev. Lett.* **2013**, *111*, 166101.
27. Dev, P.; Reinecke, T. L. Substrate Effects: Disappearance of Adsorbate-Induced Magnetism in Graphene. *Phys. Rev. B* **2014**, *89*, 035404.
28. Faizabadi, E.; Esmaeilzadeh, M.; Sattari, F. Spin Filtering in a Ferromagnetic Graphene Superlattice. *Eur. Phys. J. B* **2012**, *85*, 198.
29. Moodera, J. S.; Santos, T. S.; Nagahama, T. The Phenomena of Spin-Filtered Tunneling. *J. Phys.: Cond. Mater.* **2007**, *19*, 165202.
30. Elias, D. C.; Nair, R. R.; Mohiuddin, T. M. G.; Morozov, S. V.; Blake, P.; Halsall, M. P.; Ferrari, A. C.; Boukhvalov, D. W.; Katsnelson, M. I.; Geim, A. K.; Novoselov, K. S. Control of Graphene's Properties by Reversible Hydrogenation. *Science* **2009**, *323*, 610–613.
31. Matis, B. R.; Bulat, F. A.; Friedman, A. L.; Houston, B. H.; Baldwin, J. W. Chemically Functionalized Graphene for Bipolar Electronics. *Appl. Phys. Lett.* **2013**, *102*, 103114.
32. Jonsson-Akerman, B. J.; Escudero, R.; Leighton, C.; Kim, S.; Schuller, I. K.; Rabson, D. A. Reliability of Normal-State Current-Voltage Characteristics as an Indicator of Tunnel-Junction Barrier Quality. *Appl. Phys. Lett.* **2000**, *77*, 1870–1872.
33. D'yakonov, M. I.; Perel', V. I. In *Optical Orientation, Modern Problems in Condensed Matter Science*; Meier, F.; Zakharchenya, B.P., Eds.; North-Holland: Amsterdam, 1984; Vol. 8, p 39.
34. Lou, X.; Adelmann, C.; Crooker, S. A.; Garlid, E. S.; Zhang, J.; Reddy, K. S. M.; Flexner, S. D.; Palmstrom, C. J.; Crowell, P. A. Electrical Detection of Spin Transport in Lateral Ferromagnet-Semiconductor Devices. *Nat. Phys.* **2007**, *3*, 197–202.
35. Sze, S. M. *Physics of Semiconductor Devices*; Wiley-Interscience: New York, 1981; p 29.
36. Avsar, A.; Yang, T.-Y.; Bae, S.; Balakrishnan, J.; Volmer, F.; Jaiswal, M.; Yi, Z.; Ali, S. R.; Guntherodt, G.; Hong, B. H.; *et al.* Toward Wafer Scale Fabrication of Graphene Based Spin Valve Devices. *Nano Lett.* **2011**, *11*, 2363–2368.
37. Zhang, P.; Wu, M. W. Electron Spin Relaxation in Graphene with Random Rashba Field: Comparison of the D'yakonov-Perel' and Elliott-Yafet-Like Mechanisms. *New J. Phys.* **2012**, *14*, 033015.
38. Wang, M.; Li, C. M. Investigation of Doping Effects on Magnetic Properties of the Hydrogenated and Fluorinated Graphene Structures by Extra Charge Mimic. *Phys. Chem. Chem. Phys.* **2013**, *15*, 3786.
39. Jonker, B. T. Electrical Spin Injection and Transport in Semiconductors. In *Handbook of Spin Transport and Magnetism in Electronic Systems*; Tsymbal, E.; Zutic, I., Eds.; CRC Press−Taylor & Francis, 2012; Chapter 17, pp 329−369.
40. Nair, R. R.; Sepioni, M.; Tsai, I.-L.; Lehtinen, O.; Keinonen, J.; Krasheninnikov, A. V.; Thomson, T.; Geim, A. K.; Grigorieva, I. V. Spin-Half Paramagnetism in Graphene Induced by Point Defects. *Nat. Phys.* **2012**, *8*, 199–202.
41. Lee, W.-K.; Whitener, K. E.; Robinson, J. T.; Sheehan, P. E. Patterning Magnetic Regions in Hydrogenated Graphene *via* e-Beam Irradiation. *Adv. Mater.* **2015**, *27*, 1774–1778.
42. McCreary, K. M.; Swartz, A. G.; Han, W.; Fabian, J.; Kawakami, R. K. Magnetic Moment Formation in Graphene Detected by Scattering of Pure Spin Currents. *Phys. Rev. Lett.* **2012**, *109*, 186604.
43. Nair, R. R.; Tsai, I. L.; Sepioni, M.; Lehtinen, O.; Keinonen, J.; Krasheninnikov, A. V.; Castro Neto, A. H.; Katsnelson, M. I.; Geim, A. K.; Grigorieva, I. V. Dual Origin of Defect Magnetism in Graphene and Its Reversible Switching by Molecular Doping. *Nat. Commun.* **2013**, *4*, 2010.
44. Popinciuc, M.; Jozsa, C.; Zomer, P. J.; Tombros, N.; Veligura, A.; Jonkman, H. T.; van Wees, B. J. Electronic Spin Transport in Graphene Field-Effect Transistors. *Phys. Rev. B* **2009**, *80*, 214427.
45. Li, C. H.; van 't Erve, O. M. J.; Jonker, B. T. Electrical Injection and Detection of Spin Accumulation in Silicon at 500 K with Magnetic Metal/Silicon Dioxide Contacts. *Nat. Commun.* **2011**, *2*, 245.